

Article

Compactability Regularities Observed during Cold Uniaxial Pressing of Layered Powder Green Samples Based on Ti-Al-Nb-Mo-B and Ti-B

Pavel Bazhin ^{1,2}, Alexander Konstantinov ¹, Andrey Chizhikov ¹, Mikhail Antipov ¹, Pavel Stolin ¹, Varvara Avdeeva ^{3,*} and Anna Antonenkova ²

¹ Merzhanov Institute of Structural Macrokinetics and Materials Sciences, Russian Academy of Sciences, ul. Akademika Osipyana 8, Chernogolovka 142432, Russia; bazhin@ism.ac.ru (P.B.); konstanta@ism.ac.ru (A.K.); chij@ism.ac.ru (A.C.); mora1997@mail.ru (M.A.); jam47@mail.ru (P.S.)

² Department "Nanotechnology and Microsystem Technology," RUDN University, Miklukho-Maklaya Str. 6, Moscow 117198, Russia; antonenkova-ayu@rudn.ru

³ Kurnakov Institute of General and Inorganic Chemistry, Russian Academy of Sciences, Leninskii Prospekt 31, Moscow 119991, Russia

* Correspondence: avdeeva.varvara@mail.ru

Abstract: We determined the compactability regularities observed during the cold uniaxial pressing of layered powder green samples, taking into account factors such as composition, height, and number of Ti-B (TiB) and Ti-Al-Nb-Mo-B (TNM) layers. The following composition was chosen for the TNM layer at %: 51.85Ti-43Al-4Nb-1Mo-0.15B, while for the Ti-B layer we selected the composition wt %: Ti-B-(20, 30, 40) Ti. Green samples were made containing both 100 vol % TiB and TNM, and those taken in the following proportions, vol %: 70TiB/30TNM, 50TiB/50TNM, 30TiB/70TNM; multilayer green samples were studied in the following proportions, vol %: 35TiB/30TNM/35TiB, 25TiB/25TNM/25TiB/25TNM, 35TNM/30TiB/35TNM. Based on the obtained rheological data, we determined the rheological characteristics of the layered green samples, including compressibility modulus, compressibility coefficient, relaxation time, and limiting value of linear section deformation. These characteristics were found to vary depending on the composition, height, and number of layers. Our findings revealed that reducing the TNM content in the charge billet composition improves the compaction of powder materials under the given technological parameters of uniaxial cold pressing. Moreover, we observed that increasing the boron content and decreasing the amount of titanium in the Ti-B composition enhances the compactability of powder materials. We also established a relationship between the compaction pressure interval and the density of the layered powder green sample.

Keywords: compactability; rheological regularities; cold uniaxial pressing; layered composite materials; powder green samples; TNM; titanium boride



Citation: Bazhin, P.; Konstantinov, A.; Chizhikov, A.; Antipov, M.; Stolin, P.; Avdeeva, V.; Antonenkova, A. Compactability Regularities Observed during Cold Uniaxial Pressing of Layered Powder Green Samples Based on Ti-Al-Nb-Mo-B and Ti-B. *Metals* **2023**, *13*, 1827. <https://doi.org/10.3390/met13111827>

Academic Editor: Manoj Gupta

Received: 25 September 2023

Revised: 24 October 2023

Accepted: 29 October 2023

Published: 30 October 2023



Copyright: © 2023 by the authors. Licensee MDPI, Basel, Switzerland. This article is an open access article distributed under the terms and conditions of the Creative Commons Attribution (CC BY) license (<https://creativecommons.org/licenses/by/4.0/>).

1. Introduction

Currently, third-generation TNM alloys based on the Ti-Al (Nb, Mo) system and β -stabilized γ -alloys are of significant scientific and practical interest. These alloys have a high melting point, low density, high elastic moduli, increasing yield strength with increasing temperature, resistance to oxidation and fire, high strength/density ratio, and heat resistance. These characteristics create favorable conditions for the use of these alloys for new generation aerospace engines [1–7].

To enhance their physical and mechanical properties, these alloys are modified with a small amount of boron [8–10], which is a structure-modifying impurity in the intermetallic compound. For example, materials based on Ti-43Al-6Nb-1Mo-1Cr-(0, 0.6)B were manufactured [11], and it was observed that the addition of boron, along with a

multi-stage forging process, improves the microstructure and significantly increases the ultimate tensile strength of alloys. The utilization of novel multicomponent alloys based on titanium aluminides represents a promising method for replacing turbine blades, traditionally made from heat-resistant nickel-based superalloys, with lighter alloys in more temperature-stressed areas of a gas turbine engine.

However, the demand for heat-resistant alloys continues to grow every year, and there are prospects for enhancing the heat-resistant properties of the alloys under development. Presently, a promising approach to increase heat resistance involves reinforcing intermetallic compounds based on titanium aluminides with various strengthening phases [12–18]. Among the strengthening phases employed, titanium monoboride stands out due to its closely matched coefficient of thermal expansion ($7.2 \times 10^{-6} \text{ K}^{-1}$) and excellent chemical and thermal compatibility with the TiAl matrix [19–21]. This fact makes titanium monoboride the most suitable candidate for the development of layered composite materials (LCMs) based on TiB/TiAl(Nb,Mo)B. The deliberate design and formation of a layered composite have the potential to enhance its physical and mechanical properties [22–29].

In the study of Hao et al. [30], LCMs based on (TiB/Ti)–TiAl were fabricated using the spark plasma sintering method. These composites were created by alternately stacking layers of TiB₂/Ti powder with a thickness of 800 μm and layers of TiAl powder with a thickness of 400 μm . The starting materials consisted of (i) pre-alloyed powder Ti–47Al–2Cr–2Nb with spherical particles with an average diameter of 75 μm , (ii) powder Ti–6Al–4V with spherical particles with a diameter of 50–100 μm , and (iii) powder TiB₂ with an average particle size of 3 μm . The authors of this study discovered that the resulting composites exhibited impressive fracture toughness and flexural strength, measuring up to 51.2 MPa $\text{m}^{1/2}$ and 1456 MPa, respectively. These mechanical properties represent an increase of 293% and 108% compared to those of monolithic TiAl-based alloys. The authors attribute this enhancement in mechanical properties to the presence of TiB/Ti composite layers.

Powder metallurgy methods serve as the primary technologies for manufacturing composite materials. These methods encompass various techniques, including selective laser sintering [31–35], hot isostatic pressing [36–38], spark plasma sintering [39–42], self-propagating high-temperature synthesis (SHS) [43–46], and several other methods [47–50], wherein pressed powder green samples serve as precursors. The quality of the green sample, which encompasses factors like uniform density along its height and radius, relative density across the entire batch, and technological strength, significantly influences the physical, mechanical, and operational properties of the resulting products.

In most cases, the method of cold uniaxial pressing [51–54] is employed to create green samples. A critical aspect in both the theory and practice of cold uniaxial powder pressing is the determination of experimental relationships between the applied pressure and the density of the resulting green sample. These experimental dependencies are used to assess the compactability of selected powder materials, enabling the selection of the necessary compaction pressure to achieve a desired green sample density. To accomplish this, numerous experiments are conducted under static loading conditions using a constant compaction pressure mode.

To establish the relationship between green sample density and compaction pressure, a separate experiment was conducted for each pressure value. However, achieving identical density values for a large batch of powder green sample proves to be a challenging task. This significantly prolongs the time required to achieve the desired outcome and complicates and reduces the efficiency of the method for green sample production.

In practice, preliminary cold pressing of green samples is carried out using specialized press molds on hydraulic presses, enabling the application of a constant pressure. Nonetheless, this approach presents significant challenges because the compaction process is essentially non-stationary and the degree of compaction of the green sample continuously changes over time. In other words, when applying the same compaction pressure at different holding times under this pressure, variations in green sample densities will occur. Consequently, the density of the powder green samples, corresponding to a specific

pressure, also relies on the duration of the compaction process at that pressure. Presently, researchers must take an empirical approach to address this issue and seek optimal pressing conditions tailored to each unique case.

To determine optimal conditions for pressing powder materials, we were pioneers in introducing a rheological approach [55]. This approach considers the compaction of powder materials as non-stationary deformation processes that are influenced by rheological factors. It enables us to understand the deformation mechanisms of powder materials and ascertain their rheological properties, among other things.

The essence of the approach lies in the construction and study of rheological stress-strain relationships. Experiments are carried out at a constant strain rate. This is the most distinguishing point from traditional methods, which apply constant compaction pressure. The resulting experimental relationships remain consistent regardless of the equipment or the form of the powder green sample. Furthermore, they are obtained continuously from a single experiment. In traditional methods, these dependencies are constructed discretely, i.e., for each point it is necessary to conduct a separate experiment.

The purpose of this work is to establish the influence of the compaction pressure of powder materials, taking into account the pressing time, on the pressing characteristics depending on the composition, height, and number of layers: Ti-B (Ti-B-(20, 30, 40 wt % Ti) and Ti-Al-Nb-Mo-B (at %: 51.85Ti-43Al-4Nb-1Mo-0.15B).

2. Materials and Methods

2.1. Objects of Research

To obtain layered powder green samples, commercial powder Ti (45 μm , 99.1%), B (1 μm , 94.0%), Al (5–7 μm , 98.6%), Nb (40–63 μm , 99.9%), and Mo (5 μm , 99.1%) were used as starting reagents. These ratios were taken from the calculation of the formation in each layer during the combustion process in the mode of self-propagating high-temperature synthesis of the following compounds: in the cermet layer, TiB-(20–40) wt % Ti (hereinafter we will denote the layer as TiB, Table 1), and in the intermetallic layer, TiAl(Nb,Mo)B (hereinafter we will denote the layer as TNM). The TNM intermetallic layer was chosen with the following composition, at %: 51.85Ti-43Al-4Nb-1Mo-0.15B. Five types of powder green samples were studied; the layers were selected with the content of 100 vol % TiB and TNM, and in the following proportions, vol %: 70TiB/30TNM, 50TiB/50TNM, 30TiB/70TNM (Table 2, Figure 1). To study the characteristics of pressing multilayer powder green samples, the following ratios of each layer were taken, vol %: 35TiB/30TNM/35TiB, 25TiB/25TNM/25TiB/25TNM, and 35TNM/30TiB/35TNM (Table 3). The composition TiB-20 was taken as a model cermet layer in multilayer powder green samples. Photos of powder green samples after pressing are shown in Figures 1 and 2.

Table 1. Composition and parameters of layers in powder green samples.

Composition Designation	Content of Free Titanium, wt %	Contents of Components in Green Sample, wt %		Bulk Density (ρ_b), g/cm ³	Compact Density (ρ_c), g/cm ³	Relative Initial Density of the Mixture (ρ_{rel})
		Ti	B			
TiB-20	20	85	15	1.327	4.01782	0.330
TiB-30	30	87	13	1.253	4.07223	0.308
TiB-40	40	89	11	1.280	4.1313	0.310
TNM	-	-	-	1.389	3.9791	0.349

Table 2. Parameters of single-layer and double-layer powder green samples before and after pressing.

Composition	Green Sample Composition, vol %	Green Sample Height, mm				Green Sample Weight, g	
		Started		Final			
TiB-20/TNM	100% TNM	45	45	28.33	28.33	30.66	30.66
	0% TiB-20		-		-		-
	70% TNM	45	31.5	28.54	21.75	30.26	21.46
	30% TiB-20		13.5		6.79		8.8
	50% TNM	45	22.5	28.56	16.04	29.98	15.33
	50% TiB-20		22.5		13.2		14.65
	30% TNM	45	13.5	28.3	11.7	29.7	9.2
	70% TiB-20		31.5		16.6		20.5
	0% TNM	45	-	28.58	-	29.3	-
100% TiB-20		45		28.58		29.3	
TiB-30/TNM	100% TNM	45	45	29.19	29.19	30.66	30.66
	0% TiB-30		-		-		-
	70% TNM	45	31.5	29.01	21.65	29.76	21.46
	30% TiB-30		13.5		7.36		8.3
	50% TNM	45	22.5	28.84	16.04	29.16	15.33
	50% TiB-30		22.5		12.8		13.83
	30% TNM	45	13.5	27.76	11.7	28.56	9.2
	70% TiB-30		31.5		16.06		19.36
	0% TNM	45	-	27.11	-	27.66	-
100% TiB-30		45		27.11		27.66	
TiB-40/TNM	100% TNM	45	45	29.19	29.19	30.66	30.66
	0% TiB-40		-		-		-
	70% TNM	45	31.5	29	21.73	29.91	21.46
	30% TiB-40		13.5		7.27		8.45
	50% TNM	45	22.5	28.44	16.8	29.46	15.33
	50% TiB-40		22.5		11.64		14.13
	30% TNM	45	13.5	28.4	12.9	28.98	9.2
	70% TiB-40		31.5		15.5		19.78
	0% TNM	45	-	28.05	-	28.26	-
100% TiB-40		45		28.05		28.26	

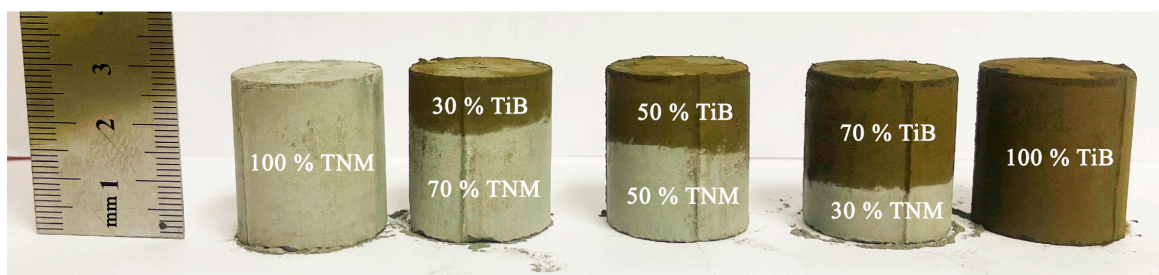
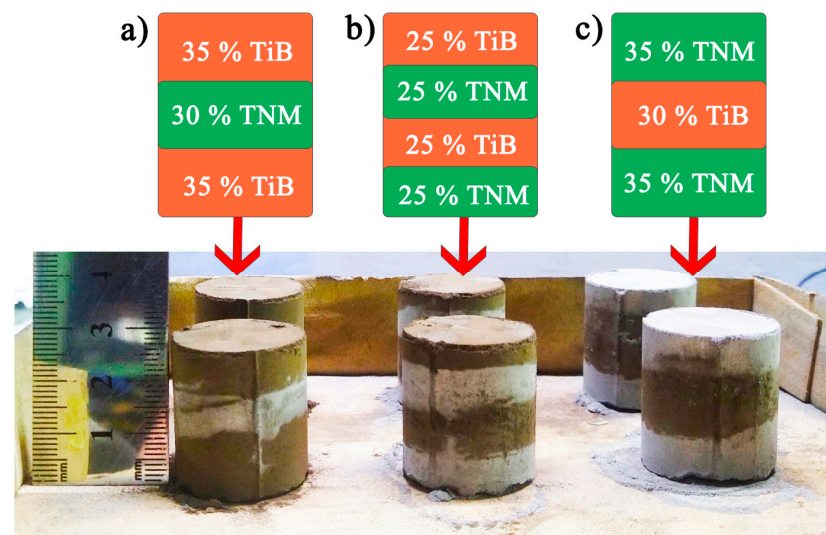
**Figure 1.** Scheme and photo of single-layer and two-layer powder green sample after pressing (composition TiB-20).

Table 3. Parameters of multilayer powder green samples before and after pressing.

Composition	Green Sample Composition, vol %	Green Sample Height, mm			Green Sample Weight, g	
		Started	Final			
35TiB/30TNM/35TiB	35% TiB-20	45	15.75	28	29.7	
	30% TNM		13.5	7.25		
	35% TiB-20		15.75	28.3		12.9
25TiB/25TNM/25TiB/25TNM	25% TiB-20	45	11.25	28.43	4.7	29.98
	25% TNM		11.25		7.13	
	25% TiB-20		11.25	28.42	8.3	
	25% TNM		11.25	28.42	8.3	
35TNM/30TiB/35TNM	35% TNM	45	15.75	28.86	10.53	30.25
	30% TiB-20		13.5	7		
	35% TNM		15.75	29.1	11.33	

**Figure 2.** Scheme (above) and photo (below) of multilayer powder green samples: (a) 35TiB/30TNM/35TiB, (b) 25TiB/25TNM/25TiB/25TNM, (c) 35TNM/30TiB/35TNM (composition TiB-20).

2.2. Research Methods

The experiments were carried out using a REM-20A compression testing machine (Metrotest, Kazan, Russia) equipped with a press mold featuring a loading chamber diameter of 25 mm. The maximum pressing force was 20 kN, and a constant deformation rate of 20 mm/min was maintained throughout all load ranges. The powder mixture under study was placed into the assembled press mold, with each bulk layer having a predefined height. The total height of the bulk layer remained fixed at 45 mm, irrespective of the proportion of the TNM and TiB layers. Details of the parameters of the charge billets before and after testing are shown in Tables 2 and 3.

The initial parameters for the research included: h_0 , the initial height of the bulk layer; m , the mass of the green sample; ρ_b , the bulk density; ρ_c , the density of the compact obtained from a non-porous powder mixture; ρ_{rel} , the relative initial density of the powder mixture. The density of the compact green sample was determined using the following Formula (1):

$$\frac{1}{\rho_c} = \sum_{i=1}^n \frac{c_i}{\rho_i} \quad (1)$$

where c_i and ρ_i are the concentration and density of the i -th component in the mixture, respectively. Relative initial density ρ_{rel} of the powder mixture was determined by the following formula: $\rho_{rel} = \rho_b / \rho_0$.

A press mold with a mixture of powders was installed under the plunger of the testing machine and loading was carried out at a constant speed of movement of the plunger to the maximum value of the pressing force (Figure 3). As a result of the experiments, “pressure–time” diagrams were constructed, which were subsequently rearranged into rheological “stress–strain” dependencies. The deformation of the powder mixture was calculated using the formula: $\varepsilon = \Delta h(t)/h_0$, where $\Delta h(t)$ is the change in the height of the bulk layer depending on the loading time. The compaction pressure was calculated as the ratio of the pressing force to the cross-sectional area of the press mold rod.

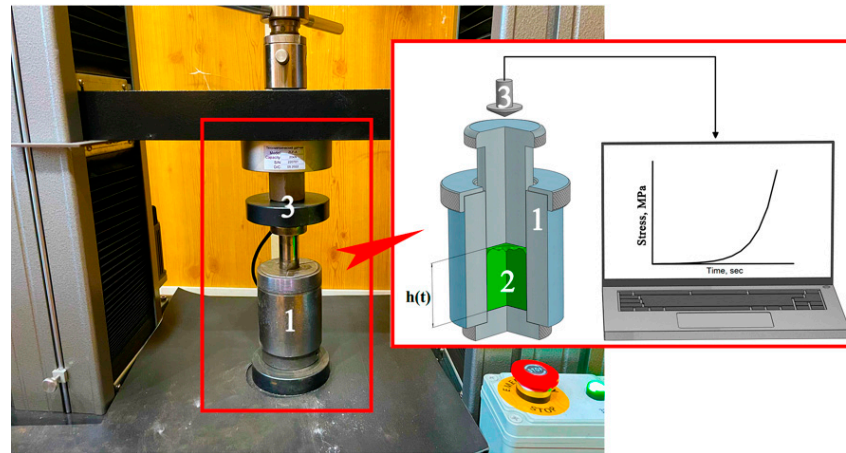


Figure 3. Photo and scheme of the experiment for determination of the compactability of powder materials: (1) press mold, (2) green sample, (3) plunger of a compression machine.

The constructed rheological dependencies have allowed us to determine the rheological characteristics of the studied powder green samples, identify the mechanisms of deformation of the powder green samples, and establish optimal compaction conditions. For the analyzed powder green samples, the following rheological characteristics were determined: the compressibility modulus (G), the limiting value of the deformation of the linear section of the rheological stress–strain relationship (ε^*), the compressibility coefficient (k_c), and the relaxation time. The limiting value of the deformation of the linear section (ε^*) characterizes the beginning of the change from the stage of elastic deformation of powder materials to elastoplastic, and it is determined by tangent of a straight line drawn from the point where pressure was applied to the resulting rheological curve. The compressibility modulus (G) is numerically equal to the tangent of the slope of the linear section of the stress–strain diagram. The compressibility coefficient (k_c) characterizes the reversible decrease in the height (volume) of a green sample under the influence of applied pressure on the “compaction pressure–change in height” diagram and is quantitatively determined by the Formula (2):

$$k_c = -\frac{1}{h_0} \cdot \frac{h'}{\Delta p'} \quad (2)$$

where $\Delta h'$ and $\Delta p'$ are the limit values for changes in height and compaction pressure in a linear section. In its physical meaning, the compressibility coefficient characterizes the ability of a material to compact at the initial (linear) stage, during which the intensity of compaction is maximum. Induction (relaxation) time is the time at which a sufficiently large pressure value is reached, the change of which has little effect on the change in the value of this parameter.

3. Results and Discussion

Figures 4–6 presents the experimental results obtained during the investigation of compaction of both single-layer and two-layer green samples. It illustrates the relationship between the pressing force and the loading time, maintaining a constant speed of move-

ment of the press plunger. Additionally, it displays the rheological curve, indicating the relationship between the deformation of powder green samples and stress. For the three compositions of the cermet layer based on Ti-B under study, the nature of the obtained dependences is similar. The intersection of the curves indicates that at the intersection points the studied green samples of different compositions have the same pressing characteristics.

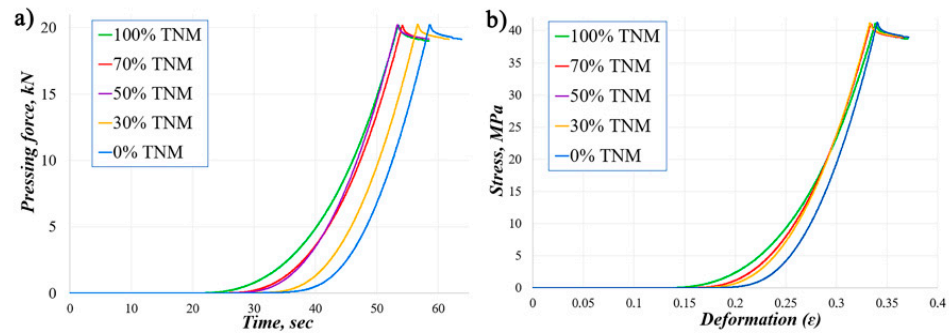


Figure 4. Experimental dependences for TiB-20/TNM compositions: (a) pressing force versus loading time; (b) rheological curve.

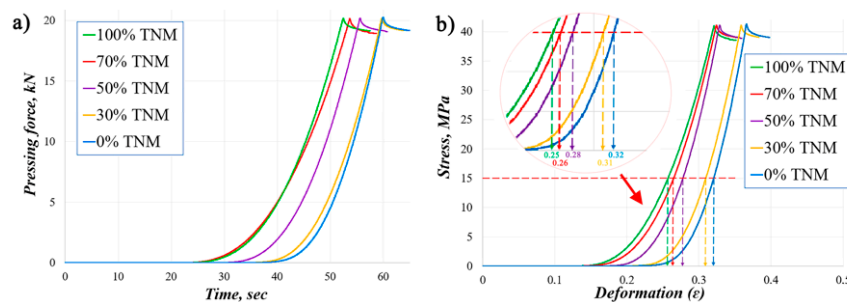


Figure 5. Experimental dependences for TiB-30/TNM compositions: (a) pressing force versus loading time; (b) rheological curve.

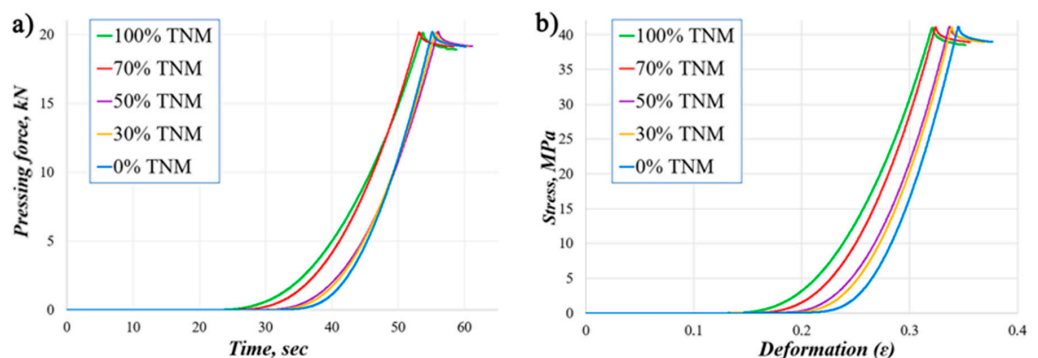


Figure 6. Experimental dependences for TiB-40/TNM compositions: (a) pressing force versus loading time; (b) rheological curve.

Let us provide an explanation of the results obtained for a cermet layer made of TiB-30. The placement of the obtained dependences is observed from left to right (relative to the reader) based on the decrease in the TNM powder content in the sample and the increase in the content of Ti-B based powder. Specifically, let us examine the scenario when the deformation stress of the studied compositions is set at 15 MPa (highlighted with a red dotted line and arrows in Figure 5). Figure 5 illustrates that for a given stress level, the degree of deformation also increases from left to right corresponding to the decrease in the TNM powder content in the green sample and the increase in the content of Ti-B based

powder: 0.25, 0.263, 0.275, 0.315, and 0.32. This indicates that the deformability of powders with increased TNM powder content is worse than that of Ti–B based powders. Specifically, for pure TNM the maximum degree of deformation did not exceed 0.325, whereas for pure Ti–B, it reached a maximum of 0.36. Therefore, depending on the content of each layer in a single-layer and two-layer green samples, the degree of deformation changes by a factor of 1.3.

The observed experimental dependencies can be elucidated by conditionally identifying three deformation sections on the rheological curves. To facilitate explanation, Figure 7 shows a scheme of the rheological curve, clearly delineating these three deformation stages.

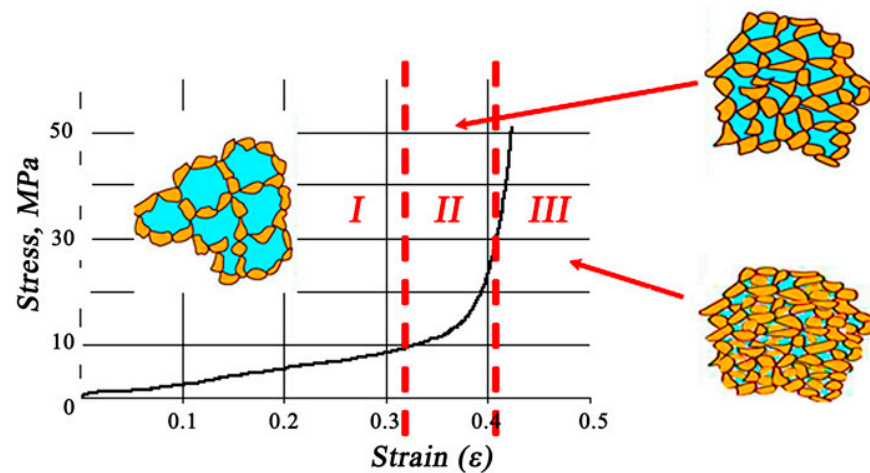


Figure 7. Three main stages of deformation of powder green samples.

The initial stage of deformation of powder materials is characterized by a linear stress increase as deformation progresses. During this stage, deformation primarily occurs due to the movement of powder particles into the pores. In coarse powder, the slope of the linear portion of the curve is more important due to the increased porosity in the green sample. When a more finely dispersed powder is deformed, the angle of inclination of the linear section of the first stage decreases, because porosity in green samples is less than when using a coarser powder. For the green sample studied, the dispersion of the powders is not high (less than 45 μm); therefore, the first section on the given scale does not look obvious. When the scale is increased, this section is clearly visible. If all the figures are marked with section numbers and enlarged scales, then the figures will not be readable, which will confuse the reader. Therefore, we have presented a generalized curve in Figure 7 for a visual explanation of the obtained dependencies.

Due to the fact that the process at the first stage occurs due to the filling of pores with powder particles, the pressing forces at this stage are low.

The second stage of deformation of powder materials exhibits a sharp, non-linear increase in stress values as deformation progresses. During this stage, the movement of particles within the studied powder occurs due to accommodation (adjustment) between them. Consequently, during this stage, the contact areas between particles increase, leading to the emergence of interatomic interaction forces in addition to their mechanical interaction. This increase in contact area and interatomic forces contributes to the overall strength of the powder green sample. This stage holds particular technological significance because it accumulates a certain amount of plastic deformation within powder green samples. However, it is essential to note that the entire powder green sample does not reach a plastic state, leading to challenges in selecting deformation conditions for porous materials.

During the third stage of deformation of powder green samples, there is a sharp increase in stress over a wide range, accompanied by only minor changes in deformation. To explain this case, we introduce a time characteristic known as the induction time (τ_i). The induction time represents the time to reach pressure, the change of which has little

effect on the values of the induction period. This time can be conventionally taken when the material moves to the third stage of the rheological “stress–strain” relationship; for each powder material studied, this value is different.

Table 4 presents the induction times for the studied compositions, demonstrating an increase as the proportion of TNM in the powder green sample. During the third stage of deformation of powder materials, the compaction primarily occurs due to the expansion of the contact surface during deformation and the brittle fracture of the particles themselves. During this stage, green sample compaction practically ceases. If stress continues to increase, it will eventually surpass the strength of the green sample, leading to its failure. Consequently, for the studied compositions, an increased proportion of TNM results in an earlier stage of brittle deformation within the particles themselves, leading to a rapid increase in compaction pressure with minimal change in the degree of deformation.

Table 4. Induction times of single-layer and double-layer powder green samples.

Composition	100%TNM	70%TNM	50%TNM	30%TNM	0%TNM
TiB-20	51.7	51.9	52.8	55.4	57.6
TiB-30	51.7	52.8	54.2	58.3	58.5
TiB-40	51.7	52.5	53.8	53.8	54.7

Table 5 displays the obtained rheological characteristics of the studied two-layer powder green sample compositions. It is evident that as the TNM content in the powder green sample decreases, the values of the compressibility modulus decrease, resulting in an increase in the values of the compressibility coefficient. Notably, the limiting values of deformation of the linear section of the rheological stress–strain relationship for the TiB-20/TNM and TiB-30/TNM compositions are nearly identical. This observation is particularly pronounced when examining the powder green samples content ranging from 50 to 100% TNM. The most significant variation in the limiting deformation value was observed for the TiB-40/TNM composition, which contains the least amount of boron.

Table 5. Rheological characteristics of single-layer and double-layer powder green samples.

Composition	100%TNM	70%TNM	50%TNM	30%TNM	0%TNM
Compressibility modulus (G), MPa					
TiB-20	5.7	4.6	4.2	3.2	2.7
TiB-30	5.7	4.3	3.8	3.1	2.4
TiB-40	5.7	4.0	3.6	3.0	1.9
Compressibility coefficient (k_c), MPa ⁻¹					
TiB-20	0.18	0.2	0.23	0.31	0.37
TiB-30	0.18	0.23	0.26	0.32	0.42
TiB-40	0.18	0.25	0.28	0.33	0.53
Limiting value of the deformation of the linear section of the rheological stress–strain relationship (ϵ^*)					
TiB-20	0.18	0.19	0.22	0.23	0.24
TiB-30	0.18	0.19	0.22	0.25	0.26
TiB-40	0.17	0.18	0.21	0.22	0.24

Based on the provided rheological patterns and calculated rheological characteristics, we can conclude that a reduction in TNM content in a two-layer powder material composition results in improved compaction under specific technological parameters of uniaxial pressing. Additionally, an increase in boron content and a decrease in titanium in the

powder green sample for Ti–B compositions leads to an improvement in the compactability of powder materials. This is attributed to the smaller boron fraction, characterized by particle sizes less than 1 μm , which more completely fills the voids in the sample during deformation.

Figure 8 presents the experimental results obtained for multilayer powder green samples, depicting the relationship between the pressing force and loading time at a constant press plunger movement speed, as well as the rheological curve, specifically, the relationship between pressing stress and strain. The observed nature of these dependencies for the studied multilayer powder green samples closely resembles that of the two-layer powder green samples.

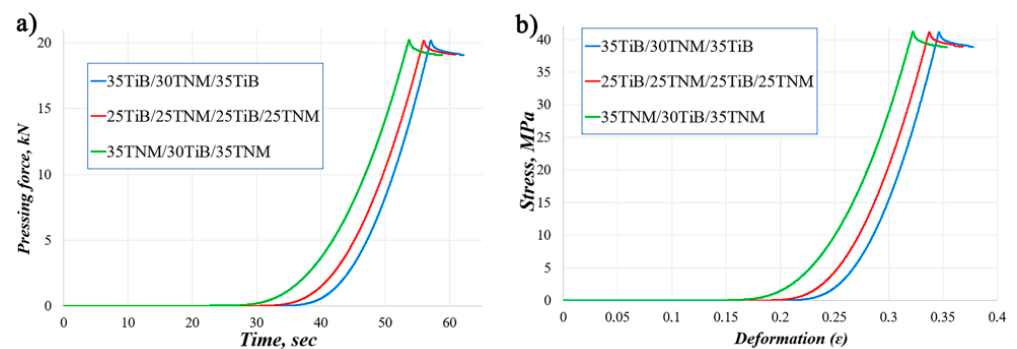


Figure 8. Experimental dependences of compaction for multilayer powder green sample: (a) pressing force versus loading time; (b) rheological “stress–strain” dependence.

To evaluate the change in the degree of deformation for each composition, we focus on the obtained values at a compaction pressure of 15 MPa. Under this constant compaction pressure, the degrees of deformation of multilayer powder green sample are as follows: 0.267, 0.287, and 0.299. Consequently, we can conclude that powder green samples composed of alternating layers for the composition 25TiB/25TNM/25TiB/25TNM exhibit the most favorable compaction ability. On the other hand, a green sample consisting of alternating layers of 35TNM/30TiB/35TNM exhibits the least favorable compaction properties. The maximum degree of deformation for multilayer green samples ranged from 0.322 to 0.347.

Drawing from the results obtained regarding the compactability of two-layer powder green samples, we can also deduce that a decrease in the TNM proportion in the powder material composition leads to improved compactability. When comparing the degree of deformation values of multilayer powder green samples with those of two-layer ones, it becomes evident that two-layer powder green samples exhibit superior compactability due to their higher content of TiB-based powder material.

Experimental dependences of the relative density of powder green samples on compaction pressure were obtained for the studied compositions (Figure 9). Since the samples consisted of layers with different densities, to calculate the average density of the green sample, the density values of each layer were taken depending on its share in the overall sample. Using the example of the TiB-40/TNM composition and the relative average density of the green sample equal to 0.45, we will provide an explanation of the obtained dependencies (Figure 9c). An increase in the proportion of TNM in the green sample leads to an increase in compaction pressure to obtain a given average density. Thus, for 100% TNM, it is necessary to apply a compaction pressure of 10 MPa, which is approximately three times higher than for pressing a green sample without TNM content. For multilayer green samples, it was found that compaction deteriorates as the amount of TNM increases (Figure 9d).

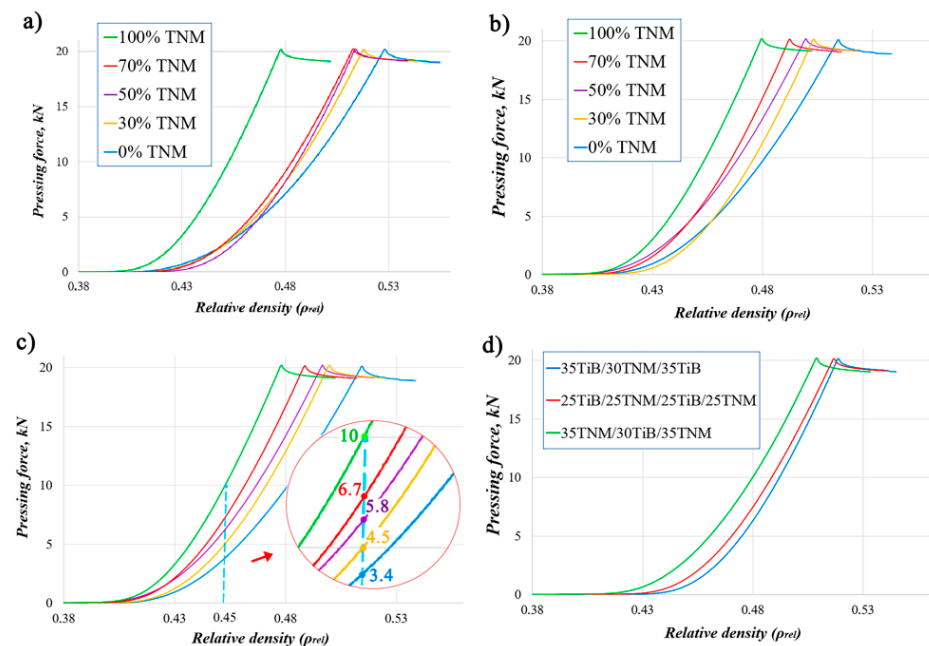


Figure 9. Dependence of relative density on compaction pressure for compositions: (a) TiB-20/TNM, (b) TiB-30/TNM, (c) TiB-40/TNM, (d) multilayer powder green sample.

The obtained experimental relationships concerning powder green sample compaction allow us to establish the connection between compaction pressure and relative density when producing samples with specific density requirements. These findings are particularly valuable in technologies where it is necessary to achieve a predefined density for the initial green sample, as this parameter significantly influences the technological parameters of the process. For instance, in self-propagating high-temperature synthesis (SHS) technologies, combustion temperature and the propagation speed of the combustion front depend significantly on relative density, which in turn determines the time duration during which the material retains its plastic properties. In spark plasma sintering technology, relative density plays a critical role in influencing sintering temperature and time.

4. Conclusions

- (1) A simple and fast method has been proposed for studying the characteristics of cold uniaxial pressing for layered powder materials. This method makes it possible to determine in one experiment the effect of compaction pressure on the density of a sample, taking into account the time of its compaction. Reducing the TNM content in the charge billet composition improves the compaction of powder materials under the given technological parameters of uniaxial cold pressing. Increasing the boron content and decreasing the amount of titanium in the Ti–B composition enhances the compactability of powder materials.
- (2) An experimental method has been proposed to ascertain the relationship between the degree of deformation and the relative density of powder green samples in relation to compaction pressure and the duration of pressure application. This method applies to single-layer, double-layer, and multilayer materials based on Ti–B–(20, 30, 40) wt % Ti and TNM (at %: 51.85Ti–43Al–4Nb–1Mo–0.15B).
- (3) Rheological patterns were studied during cold uniaxial pressing of powder green samples depending on the composition of the initial components, height, and number of layers Ti–B–(20, 30, 40) wt % Ti and TNM (at %: 51.85Ti–43Al–4Nb–1Mo–0.15B). Layers were selected containing both 100 vol % TiB and TNM, and the following proportions: 70TiB/30TNM, 50TiB/50TNM, 30TiB/70TNM. In addition, multilayers were also studied in the following proportions: vol %: 35TiB/30TNM/35TiB, 25TiB/25TNM/25TiB/25TNM, and 35TNM/30TiB/35TNM. Based on the obtained

rheological patterns and calculated rheological characteristics, it was concluded that with a decrease in the TNM content in the composition of the powder green sample, the compaction of powder materials at given technological parameters of uniaxial pressing improves.

- (4) It was found that an increase in boron content and a decrease in titanium content in the composition of the Ti–B powder layer leads to an improvement in the compactability of powder materials. This improvement is attributed to the more effective filling of pore space in the powder green sample by finely dispersed boron powder, surpassing the performance of other components.
- (5) The obtained experimental relationships on powder green sample compaction facilitated the establishment of a correlation between compaction pressure and relative density, which is associated with pressing time.

Author Contributions: P.B.: Conceptualization, Methodology; Writing—Review & Editing; A.K.: Formal analysis; A.C.: Formal analysis, Visualization; M.A.: Investigation; P.S.: writing—original draft preparation; V.A.: Writing—Review & Editing; A.A.: Visualization. All authors have read and agreed to the published version of the manuscript.

Funding: This work was supported by the Russian Science Foundation, grant no. 22-19-00040, <https://rscf.ru/project/22-19-00040> (Russia, accessed on 24 October 2023).

Data Availability Statement: Data sharing is not applicable to this article.

Acknowledgments: This work was carried out using the equipment of the Distribution Center for Collective Use of the Merzhanov Institute (ISMAN).

Conflicts of Interest: The authors declare that they have no known competing financial interest or personal relationships that could have appeared to influence the work reported in this paper.

References

1. Yingmei, T.; Ruirun, C.; Hongze, F.; Yangli, L.; Hongzhi, C.; Yanqing, S.; Jingjie, G.; Hengzhi, F. Enhanced strength and ductility in Ti₄₆Al₄Nb₁Mo alloys via boron addition. *J. Mater. Sci. Technol.* **2022**, *102*, 16–23. [[CrossRef](#)]
2. Ruxin, C.; Xicong, Y.; Renci, L.; Xi, W.; Chao, Y.; Dong, L.; Yuyou, C.; Rui, Y. Influence of section thickness of casting on the microstructure characteristics and creep rupture properties of Ti-45Al-2Nb-2Mn-1B. *Mater. Charact.* **2023**, *202*, 113056. [[CrossRef](#)]
3. Shaaban, A.; Hayashi, S.; Takeyama, M.A. Comparative study on the oxidation behaviours of a TNM alloy in argon and oxygen atmospheres at 650 degrees. *Corros. Sci.* **2021**, *185*, 109415. [[CrossRef](#)]
4. Galetz, M.C.; Ulrich, A.S.; Oskay, C. Oxidation-induced microstructural changes of the TiAl TNM-B1 alloy after exposure at 900 °C in air. *Intermetallics* **2020**, *123*, 106830. [[CrossRef](#)]
5. Nazarova, T.; Nazarov, K.; Sergeev, S.; Imayev, V.; Imayev, R. Microstructure and mechanical properties of intermetallic γ -TiAl alloy alloyed with dysprosium. *Lett. Mater.* **2017**, *7*, 307–311. [[CrossRef](#)]
6. Siyu, C.; Yingmei, T.; Xuan, W.; Feng, C.; Liang, W.; Yanqing, S.; Jingjie, G. Individual and synergistic effects of Ta and Mn on optimizing the microstructures and mechanical properties of TiB reinforced high Nb–TiAl composites. *J. Mater. Res. Technol.* **2023**, *23*, 209–220. [[CrossRef](#)]
7. Xiuxuan, Y.; Zhang, B. Correlation of microstructure and mechanical properties of Ti₂AlNb manufactured by SLM and heat treatment. *Intermetallics* **2021**, *139*, 107367. [[CrossRef](#)]
8. Malinina, E.A.; Myshletsov, I.I.; Buzanov, G.A.; Kubasov, A.S.; Kozerozhets, I.V.; Goeva, L.V.; Nikiforova, S.E.; Avdeeva, V.V.; Zhizhin, K.Y.; Kuznetsov, N.T. A New Approach to the Synthesis of Nanocrystalline Cobalt Boride in the Course of the Thermal Decomposition of Cobalt Complexes [Co(DMF)₆]²⁺ with Boron Cluster Anions. *Molecules* **2023**, *28*, 453. [[CrossRef](#)]
9. Sivaev, I.B. Decaborane: From Alfred Stock and Rocket Fuel Projects to Nowadays. *Molecules* **2023**, *28*, 6287. [[CrossRef](#)]
10. Avdeeva, V.V.; Nikiforova, S.E.; Malinina, E.A.; Sivaev, I.B.; Kuznetsov, N.T. Composites and Materials Prepared from Boron Cluster Anions and Carboranes. *Materials* **2023**, *16*, 6099. [[CrossRef](#)]
11. Xiao, S.; Chen, Y.; Li, M. The improved properties and microstructure of β -solidify TiAl alloys by boron addition and multi steps forging process. *Sci. Rep.* **2019**, *9*, 12393. [[CrossRef](#)] [[PubMed](#)]
12. Cui, S.; Cui, C.; Wang, X. Microstructure and Mechanical Properties of Dual Scaled NbC/Ti₂AlC Reinforced Titanium–Aluminum Composite. *Materials* **2023**, *16*, 4661. [[CrossRef](#)] [[PubMed](#)]
13. Fu, Z.; Mondal, K.; Koc, R. Sintering, mechanical, electrical and oxidation properties of ceramic intermetallic TiC–Ti₃Al composites obtained from nano-TiC particles. *Ceram. Int.* **2016**, *42*, 9995–10005. [[CrossRef](#)]
14. Wang, J.; Kong, L.; Li, T.; Xiong, T. A novel TiAl₃/Al₂O₃ composite coating on γ -TiAl alloy and evaluating the oxidation performance. *Appl. Surf. Sci.* **2016**, *361*, 90–94. [[CrossRef](#)]

15. Zhao, J.; Li, Q.; Cao, W.; Liu, Z.; Deng, X.; Ding, X.; Ran, S. Influences of B₄C content and particle size on the mechanical properties of hot pressed TiB₂-B₄C composites. *J. Asian. Ceram. Soc.* **2021**, *9*, 1239–1247. [[CrossRef](#)]
16. Li, X.; Xie, X.; Gonzalez-Julian, J.; Malzbender, J.; Yang, R. Mechanical and oxidation behavior of textured Ti₂AlC and Ti₃AlC₂ MAX phase materials. *J. Eur. Ceram. Soc.* **2020**, *40*, 5258–5271. [[CrossRef](#)]
17. Cai, C.; Radoslaw, C.; Zhang, J.; Yan, Q.; Wen, S.; Song, B.; Shi, Y. In-situ preparation and formation of TiB/Ti-6Al-4V nanocomposite via laser additive manufacturing: Microstructure evolution and tribological behavior. *Powder Technol.* **2019**, *342*, 73–84. [[CrossRef](#)]
18. Avdeeva, V.; Bazhina, A.; Antipov, M.; Stolin, A.; Bazhin, P. Relationship between Structure and Properties of Intermetallic Materials Based on γ -TiAl Hardened In Situ with Ti₃Al. *Metals* **2023**, *13*, 1002. [[CrossRef](#)]
19. Namini, A.S.; Azadbeh, M.; Asl, M.S. Effect of TiB₂ content on the characteristics of spark plasma sintered Ti-TiBw composites. *Adv. Powder Technol.* **2017**, *28*, 1564–1572. [[CrossRef](#)]
20. Hou, J.; Gao, L.; Cui, G.; Chen, W.; Zhang, W.; Tian, W. Grain Refinement of Ti-15Mo-3Al-2.7Nb-0.2Si Alloy with the Rotation of TiB Whiskers by Powder Metallurgy and Canned Hot Extrusion. *Metals* **2020**, *10*, 126. [[CrossRef](#)]
21. Bazhin, P.; Stolin, A.; Konstantinov, A.; Kostitsyna, E.; Ignatov, A. Ceramic Ti-B Composites Synthesized by Combustion Followed by High-Temperature Deformation. *Materials* **2016**, *9*, 1027. [[CrossRef](#)] [[PubMed](#)]
22. Bazhin, P.M.; Konstantinov, A.S.; Chizhikov, A.P.; Pazniak, A.I.; Kostitsyna, E.V.; Prokopets, A.D.; Stolin, A.M. Laminated cermet composite materials: The main production methods, structural features and properties (review). *Ceram. Int.* **2021**, *47*, 1513–1525. [[CrossRef](#)]
23. Denisov, I.; Shakhrai, D.; Malakhov, A.; Seropyan, S. Combustion Synthesis of Metal-Intermetallic-Ceramic Laminate AlMg₆-NiAl-TiC Composite. *Crystals.* **2022**, *12*, 1851. [[CrossRef](#)]
24. Liu, J.; Li, P.; Huai, Y. Interface Characteristics and Mechanical Properties of Post-treated Directed Energy Deposition Laminated Composites. *J. Mater. Eng. Perform.* **2023**, *32*, 7260–7274. [[CrossRef](#)]
25. Prokopets, A.; Bazhin, P.; Konstantinov, A.; Chizhikov, A.; Antipov, M.; Avdeeva, V. Structural features of layered composite material TiB₂/TiAl/Ti₆Al₄V obtained by unrestricted SHS-compression. *Mater. Lett.* **2021**, *300*, 130165. [[CrossRef](#)]
26. Bazhina, A.; Konstantinov, A.; Chizhikov, A.; Bazhin, P.; Stolin, A.; Avdeeva, V. Structure and mechanical characteristics of a layered composite material based on TiB/TiAl/Ti. *Ceram. Int.* **2022**, *48*, 14295–14300. [[CrossRef](#)]
27. Bazhin, P.; Chizhikov, A.; Bazhina, A.; Konstantinov, A.; Avdeeva, V. Titanium-titanium boride matrix composites prepared in-situ under conditions combining combustion processes and high-temperature shear deformation. *Mater. Sc. Eng. A* **2023**, *874*, 145093. [[CrossRef](#)]
28. Khvostunkov, K.; Bazhin, P.; Ni, Q.-Q.; Bazhina, A.; Chizhikov, A.; Konstantinov, A. Influence of Layer-Thickness Proportions and Their Strength and Elastic Properties on Stress Redistribution during Three-Point Bending of TiB/Ti-Based Two-Layer Ceramics Composites. *Metals* **2023**, *13*, 1480. [[CrossRef](#)]
29. Hao, D.; Xiping, C.; Naonao, G.; Yuan, S.; Yuanyuan, Z.; Lujun, H.; Lin, G. Fabrication of (TiB/Ti)-TiAl composites with a controlled laminated architecture and enhanced mechanical properties. *J. Mater. Sci. Technol.* **2021**, *62*, 221–233. [[CrossRef](#)]
30. Sanqiang, X.; Bailu, L.; Zhengxing, L.; Xiaokang, Y. Microstructures and mechanical behaviors of reinforced aluminum matrix composites with modified nano-sized TiB₂/SiC fabricated by selective laser melting. *Compos. Commun.* **2023**, *37*, 101439. [[CrossRef](#)]
31. Gao, C.; Liu, Z.; Xiao, Z.; Zhang, W.; Wong, K.; Akbarzadeh, A.H. Effect of heat treatment on SLM-fabricated TiN/AlSi₁₀Mg composites: Microstructural evolution and mechanical properties. *J. Alloys Compd.* **2021**, *853*, 156722. [[CrossRef](#)]
32. Zacharatos, F.; Karvounis, P.; Theodorakos, I.; Hatziapostolou, A.; Zergioti, I. Single Step Laser Transfer and Laser Curing of Ag NanoWires: A Digital Process for the Fabrication of Flexible and Transparent Microelectrodes. *Materials* **2018**, *11*, 1036. [[CrossRef](#)] [[PubMed](#)]
33. Zhou, P.; Qi, H.; Zhu, Z.; Qin, H.; Li, H.; Chu, C.; Yan, M. Development of SiC/PVB Composite Powders for Selective Laser Sintering Additive Manufacturing of SiC. *Materials* **2018**, *11*, 2012. [[CrossRef](#)] [[PubMed](#)]
34. Polozov, I.; Gracheva, A.; Popovich, A. Interface Characterization of Bimetallic Ti-6Al-4V/Ti₂AlNb Structures Prepared by Selective Laser Melting. *Materials* **2022**, *15*, 8528. [[CrossRef](#)] [[PubMed](#)]
35. Becker, L.; Lentz, J.; Kramer, B.; Rottstegge, A.; Broeckmann, C.; Theisen, W.; Weber, S. Validation of the Powder Metallurgical Processing of Duplex Stainless Steels through Hot Isostatic Pressing with Integrated Heat Treatment. *Materials* **2022**, *15*, 6224. [[CrossRef](#)] [[PubMed](#)]
36. Soliman, H.A.; Pineault, J.; Elbestawi, M. Influence of Combined Heat Treatment and Hot Isostatic Pressure (HT-HIP) on Titanium Aluminide Processed by L-PBF. *Materials* **2023**, *16*, 5071. [[CrossRef](#)]
37. Kaletsch, A.; Sondermann, M.; Mirz, M.; Radtke, F.; Broeckmann, C. Influence of PBF-LB Process Atmosphere on the Fatigue Strength of Hot Isostatically Post-Densified Duplex Steel Parts Produced via the Shell Core Approach. *Materials* **2023**, *16*, 4014. [[CrossRef](#)]
38. Hu, B.; Cai, G. Effect of Hot Isostatic Pressing Process Parameters on Properties and Fracture Behavior of Tungsten Alloy Powders and Sintered Bars. *Materials* **2022**, *15*, 8647. [[CrossRef](#)]
39. Wimler, D.; Lindemann, J.; Clemens, H.; Mayer, S. Microstructural Evolution and Mechanical Properties of an Advanced γ -TiAl Based Alloy Processed by Spark Plasma Sintering. *Materials* **2019**, *12*, 1523. [[CrossRef](#)]

40. Musi, M.; Deshayes, C.; Molénat, G.; Toualbi, L.; Galy, B.; Spoerk-Erdely, P.; Hantcherli, M.; Monchoux, J.-P.; Thomas, M.; Clemens, H. Microstructure, Plasticity and Ductility of a TNM+ Alloy Densified by Spark Plasma Sintering. *Metals* **2022**, *12*, 1915. [[CrossRef](#)]
41. Zhichao, L.; Yanguo, L.; Qin, Z.; Wenqi, L.; Haotian, G.; Zhuang, L.; Yong'an, L. In-situ fabrication and characterization of TiC matrix composite reinforced by SiC and Ti₃SiC₂. *Ceram. Int.* **2023**, *49*, 20849–20859. [[CrossRef](#)]
42. Zhichao, L.; Yanguo, L.; Qin, Z.; Wenqi, L.; Haotian, G.; Zhuang, L.; Yong'an, L. Fabrication of the TiC matrix composite with the intragranular Al₂O₃ using carbon fibers as carbon source. *Mater. Charact.* **2023**, *199*, 112817. [[CrossRef](#)]
43. Loginov, P.A.; Kaplanskii, Y.Y.; Markov, G.M.; Patsera, E.I.; Vorotilo, K.V.; Korotitskiy, A.V.; Shvyndina, N.V.; Levashov, E.A. Structural and mechanical properties of Ti–Al–Nb–Mo–B alloy produced from the SHS powder subjected to high-energy ball milling. *Mater. Sci. Eng. A* **2021**, *814*, 141153. [[CrossRef](#)]
44. Bin, Y.; Tiechui, Y.; Junjie, S.; Yuchao, Q.; Chenglong, J.; Xiaoping, W.; Daihong, X.; Ruidi, L.; Han, J.; Mingfeng, Y. Preparation of high-quality FeV50 alloy by an improved SHS-EAH multi-stage process. *Ceram. Int.* **2023**, *49*, 15114–15121. [[CrossRef](#)]
45. Evseev, N.S.; Matveev, A.E.; Nikitin, P.Y. Synthesis, Structure, and Phase Composition of High-Entropy Ceramics (HfTiCN)-TiB₂. *Russ. J. Inorg. Chem.* **2022**, *67*, 1319–1323. [[CrossRef](#)]
46. Bazhin, P.; Konstantinov, A.; Chizhikov, A.; Prokopets, A.; Bolotskaia, A. Structure, physical and mechanical properties of TiB-40 wt.% Ti composite materials obtained by unrestricted SHS compression. *Mater. Today Com.* **2020**, *25*, 101484. [[CrossRef](#)]
47. Nasakina, E.O.; Sudarchikova, M.A.; Demin, K.Y.; Mikhailova, A.B.; Sergienko, K.V.; Konushkin, S.V.; Kaplan, M.A.; Baikin, A.S.; Sevostyanov, M.A.; Kolmakov, A.G. Study of Co-Deposition of Tantalum and Titanium during the Formation of Layered Composite Materials by Magnetron Sputtering. *Coatings* **2023**, *13*, 114. [[CrossRef](#)]
48. Kabaldin, Y.; Shatagin, D.; Ryabov, D.; Solovyov, A.; Kurkin, A. Microstructure, Phase Composition, and Mechanical Properties of a Layered Bimetallic Composite ER70S-6-ER309LSI Obtained by the WAAM Method. *Metals* **2023**, *13*, 851. [[CrossRef](#)]
49. Malyutina, Y.N.; Anisimov, A.G.; Popelyukh, A.I.; Lozhkin, V.S.; Bataev, A.A.; Bataev, I.A.; Lukyanov, Y.L.; Pai, V.V. Microstructure and Properties of Multilayer Niobium-Aluminum Composites Fabricated by Explosive Welding. *Metals* **2022**, *12*, 1950. [[CrossRef](#)]
50. Guo, J.; Chen, W.; Du, D.; Zhang, W.; Cui, G.; Yang, J. Temperature influenced microstructure evolution and strengthening of 4.5 vol% TiBw/TA15 composites with columnar-reinforced structure fabricated by pre-sintering and hot extrusion. *Mater. Charact.* **2022**, *190*, 112017. [[CrossRef](#)]
51. Gómez-Rodríguez, C.; Fernández-González, D.; García-Quirñonez, L.V.; Castillo-Rodríguez, G.A.; Aguilar-Martínez, J.A.; Verdeja, L.F. MgO Refractory Doped with ZrO₂ Nanoparticles: Influence of Cold Isostatic and Uniaxial Pressing and Sintering Temperature in the Physical and Chemical Properties. *Metals* **2019**, *9*, 1297. [[CrossRef](#)]
52. Feijoo, I.; Cabeza, M.; Merino, P.; Pena, G.; Rey, P. Age Hardening of Extruded AA 6005A Aluminium Alloy Powders. *Materials* **2019**, *12*, 2316. [[CrossRef](#)] [[PubMed](#)]
53. Peter Martin, L.; Andrea, M.; Geoffrey, H. Compaction behavior of uniaxially cold-pressed Bi–Ta composites. *Scr. Mater.* **2007**, *57*, 229–232. [[CrossRef](#)]
54. Muhammad, I.A.K.; Mohammad, S.M.; Noradila, A.L.; Ahmed, S.M. Microstructural Analysis and Mechanical Properties of Direct Recycling Aluminium Chips AA6061/Al Powder Fabricated by Uniaxial Cold Compaction Technique. *Procedia Eng.* **2017**, *184*, 687–694. [[CrossRef](#)]
55. Stolin, A.M.; Bazhin, P.M.; Pugachev, D.V. Cold uniaxial compaction of Ti-containing powders: Rheological aspects. *SHS* **2008**, *17*, 154–155. [[CrossRef](#)]

Disclaimer/Publisher’s Note: The statements, opinions and data contained in all publications are solely those of the individual author(s) and contributor(s) and not of MDPI and/or the editor(s). MDPI and/or the editor(s) disclaim responsibility for any injury to people or property resulting from any ideas, methods, instructions or products referred to in the content.